ROYAL SOCIETY OF CHEMISTRY

PAPER

Check for updates

Crystallization dynamics and stabilization of FAPbI₃ single-phase perovskite†

Weiwei Zuo, [ID] [a] Weifei Fu, [b] Ke Wang, [ID] [c] Chittarajan Das, [af]
Mahdi Malekshahi Byranvand, [ID] [af] Kai-Li Wang, [d] Aditya Chaudhary, [a] Jaekeun Lim, [a]
Meng Li*[e] and Michael Saliba [ID] *[af]

The fundamental ABX₃ structure of metal-halide perovskites is crucial for maintaining the crystal lattice stability and also enables exceptional optoelectronic properties. One main goal of the research community is to produce phase-stable ("black phase") FAPbI₃. Here, we used the LaMer model and an *in situ* optical microscope to investigate the perovskite crystallization process. We aim to develop a stable (black) single-phase FAPbI₃ perovskite by investigating the $[PbX_6]^{4-}$ template and associated A-cations. Specifically, the addition of MACl is shown to facilitate the crystallization of FAPbI₃ without changing the $[PbI_6]^{4-}$ skeleton. On the other hand, MABr acts as a passivation agent for the film, resulting in stable FAPbI₃ films with a pure black phase when exposed to air with a humidity of 45%.

Broader context

The development of perovskite solar cells (PSCs), a rapidly emerging technology in photovoltaics, has attracted significant attention worldwide. They have achieved efficiencies comparable to silicon solar cells in just a decade. However, a deeper understanding of the crystallization process for perovskite thin films is still required to advance further. Controlling the crystallization process plays a crucial role in creating high-quality films. Our research determines that FAPbI₃ has the longest crystallization formation time among the single-components of metal-halide perovskites. At the same time, it tends to form the hexagonal, non-perovskite polymorph, which is not suitable for photovoltaic applications. Through an in-depth exploration of the perovskite crystallization process, we introduce a strategy to produce stable black single-phase FAPbI₃ films for high-performance PSCs. In contrast to the many heterogeneous additives and passivators, our selection of homogeneous additives/passivators was guided by analyzing the crystallization mechanism in depth. Based on this, we successfully produced FAPbI₃ films that were more stable than the control devices.

[a] *Institute for Photovoltaics (ipv), University of Stuttgart, Pfaffenwaldring 47 D-70569 Stuttgart, Germany. E-mail: michael.saliba@ipv.uni-stuttgart.de*

[b] *State Key Laboratory of Silicon and Advanced Semiconductor Materials, International Research Center for X Polymers, Shanxi-Zheda Institute of Advanced Materials and Chemical Engineering, Department of Polymer Science and Engineering, Zhejiang University, Hangzhou 310027, P. R. China*

[c] *Institute for Materials Science, University of Stuttgart, Heisenbergstr. 3, 70569 Stuttgart, Germany*

[d] *Institute of Functional Nano & Soft Materials (FUNSOM), Jiangsu Key Laboratory for Carbon-Based Functional Materials & Devices, Soochow University, Suzhou, Jiangsu 215123, China*

[e] *Key Lab for Special Functional Materials of Ministry of Education, National & Local Joint Engineering Research Center for High-efficiency Display and Lighting Technology, School of Materials Science and Engineering, Collaborative Innovation Center of Nano Functional Materials and Applications, Henan University, Kaifeng 475004, China. E-mail: mengli@henu.edu.cn*

[f] *Helmholtz Young Investigator Group FRONTRUNNER, IEK5-Photovoltaics Forschungszentrum Jülich, 52425 Jülich, Germany*

† Electronic supplementary information (ESI) available. See DOI: https://doi.org/10.1039/d3ee02404k

Introduction

Perovskite solar cells (PSCs) have achieved an excellent power conversion efficiency (PCE) of 26.1%,[1] which can be attributed to an exceptional light absorption coefficient,[2] low Urbach energy,[3] long carrier diffusion length,[4] and defect tolerance.[5] These materials have the generic formula "ABX₃", where A is a monovalent cation such as Cs, methylammonium (MA) or formamidinium (FA), B is a divalent metal cation such as Pb or Sn, and X is a halide anion such as Cl, Br or I. They consist of $[BX_6]^{4-}$ octahedra that form a three-dimensional (3D) structure.[6–9] These corner-sharing $[BX_6]^{4-}$ octahedra leave voids, where the A cations reside. As the A-cations do not interact strongly with the metal-halide octahedra,[10–12] the $[BX_6]^{4-}$ structure acts as a "skeleton" or scaffold.

In multi-component perovskites, the different ionic radii of I⁻, Br⁻, and Cl⁻ lead to different miscibility between the $[PbX_6]^{4-}$ sublattices, especially between I⁻ and Cl⁻.[13] The different ionic radii will also influence the bond length.

For example, the Pb–Br bond length is 3.067 Å, whereas the Pb–I bond length is 3.279 Å.[14] This can cause stacking faults in the lattice, leading to potential crystallographic defects.

However, the complexities of multi-phase or multi-component perovskites can be remedied through a controlled crystallization process of single-component perovskite films. For example, Peng *et al.* fabricated single-crystal $MAPbBr_3$[15] and $MAPbI_3$[16] solar cells with PCEs of 6.53% and 21.1% respectively. However, single crystal thin films[15,17–22] are arduous to fabricate and may be impractical for industrial manufacturing. Hence, fabricating perovskite films with a simpler method would be desirable, where the stability of the single-phase perovskite is maintained.

Therefore, in this work, we focus on the growth of stable black single-phase $FAPbI_3$ perovskite. After analysing the crystallization formation time of various perovskites, we chose MACl as a crystallizing aid, which can be removed at relative ease due to its low boiling point,[23,24] making it an ideal choice for single-phase perovskite growth. Furthermore, the post-treatment with MABr introduces MA^+ ions to repair defects in $FAPbI_3$ films, while Br^- ions could enhance the film stability. Notably, the modified perovskite films by MABr exhibit higher stability compared to the MABr-free perovskite films. The corresponding solar cell exhibits a PCE of 23.0%.

Results and discussion

The crystallization process of perovskites can be mapped to a LaMer model (see Fig. 1a) as reported in literature[25–27] (the process is described in Supplementary Note 1, ESI†). The LaMer model is a first approximation for the crystallization behavior providing a general overview of the process. As the complex role of the additives in the perovskite precursor is studied in more detail, the LaMer model may need modification and adjustment in future studies accounting for these complexities. To map the crystallization formation time (t_{form}), according to the LaMer model, the *in situ* crystallization process is recorded by an optical microscope as shown in Fig. 1b. Here, as an example, we show images of the time sequence of the crystallization process of $FAPbI_3$ (the overall video and all other videos are shown in the ESI.† Also, the film fabrication conditions are described in Supplementary Note 2, ESI†).

From this, we determine the t_{form} to go from t_3 to t_4. t_3 marks the moment when nuclei become visible. This occurrence is a result of varying growth times for microcrystalline particles in the film. When observing the film through an optical microscope, the first microcrystalline particle becomes apparent at t_3, and we define this time as the point when nuclei appear. t_4 is the approximate time at which we cannot readily observe the change in crystal growth any longer. The t_{form} comparison is shown in Fig. 1c–e, the crystallization process is shown in the ESI,† the videos and the values of the crystallization times are shown in Table S1 (ESI†).

We then investigate perovskite films containing different A-cations at equimolar concentrations to study the impact of

the cation radius on the t_{form}. Cs^+, MA^+, and FA^+ are selected as the most commonly used A-cations (with the size increasing as Cs^+ (1.81 Å) $<$ MA^+ (2.70 Å) $<$ FA^+ (2.79 Å)).[28,29]

As depicted in Fig. 1c, a notable increase in t_{form} is observed as the A-cation size increases from Cs^+ to FA^+ in $FA_xCs_{1-x}PbI_3$ from 33 s ($Cs_{0.5}FA_{0.5}PbI_3$) to more than 600 s with $x > 0.5$, where x is the mole ratio of FA^+ to all the A-cations in the precursor. Conversely, the t_{form} decreases from 237 s ($MA_{0.2}FA_{0.8}PbI_3$) to 49 s ($MA_{0.5}FA_{0.5}PbI_3$) as the MA^+ concentration exceeded 50% in $MA_xFA_{1-x}PbI_3$. We note that the short t_{form} of $CsPbI_3$ made it challenging to determine the crystallization time, which is consistent with previous reports.[30] As the size of the A-cation in perovskites increases from Cs^+ to MA^+ to FA^+, the t_{form} increases (*e.g.* t_{form} of $MAPbI_3$ is 39 s and $FAPbI_3$ is 620 s), with the longest t_{form} observed for FA^+ and the shortest t_{form} observed for Cs^+.

Moreover, we also study the impact of the halogen size on t_{form} (Fig. 1d). For $MAPbI_{3-x}Cl_x$, the t_{form} of the perovskite increase significantly when $x > 0.2$ as the Cl^- ratio increases from 22 s ($MAPbI_{2.8}Cl_{0.2}$) to 73 s ($MAPbI_2Cl$), where x is the mole ratio of Cl^- to all the halogens in the precursor. For $MAPbI_2Br_{1-x}Cl_x$, the t_{form} becomes shorter with higher Br content (*e.g.* t_{form} of $MAPbI_2Cl$ is 73 s and $MAPbI_2Br$ is 45 s). However, when the Cl content is further decreased beyond $x <$ 0.5, the t_{form} increases from 22 s ($MAPbI_{2.9}Cl_{0.1}$) to 28 s ($MAPbI_3$), indicating that additional factors may affect t_{form}. For example, the number of ionic species and the number of ions in the perovskite precursors. Even so, when we replace halogens in equal proportions, comparing $MAPbI_3$, $MAPbI_2Br$ and $MAPbI_2Cl$, it is evident that the t_{form} follows t_{MAPbI_3}(28 s) $<$ t_{MAPbI_2Br} (45 s) $<$ t_{MAPbI_2Cl} (73 s), which indicates that the larger the radius of the halogen atom the shorter the crystallization time. This regular pattern changes when both the A cation and the halogen are varied, as in Fig. 1e. It suggests when the ionic species become more complicated (possibly due to the increased combinations when mixing), which may also affect t_{form}. However, this goes beyond the scope of the current work as it requires multivariable analysis. Nevertheless, we can still see that in $(MAPbI_2Cl)_x(FAPbI_3)_{1-x}$, the addition of an appropriate concentration of MACl to $FAPbI_3$ results in a longer t_{form} for $FAPbI_3$ (*e.g.* t_{form} of $(MAPbI_2Cl_2)_{0.1}(FAPbI_3)_{0.9}$ is 747 s compare to $FAPbI_3$ with 555 s). Based on our observations, in lead-based perovskite, it can be inferred that the t_{form} will be longer when as r_A increases or r_x decreases (A = Cs, MA, FA; X= Cl, Br, I).

The A-cation strongly influences the perovskite crystallization, as it affects the t_{form} and determines whether a relatively stable intermediate phase can be obtained. To investigate the diffusion of A cations in the PbI_2 lattice, $FA_xMA_{1-x}PbI_3$ films are fabricated without antisolvent and kept in a nitrogen atmosphere for three days to ensure the end of spontaneous crystallization as shown in Fig. 2. Subsequently, one of the films is annealed at 100 °C for 10 min while the other is used as the control sample. The $FAPbI_3$ film retains its yellow phase color after being kept in nitrogen for three days without annealing. However, as the percentage of MA in the perovskite is gradually increased, the color of the film changes from yellow
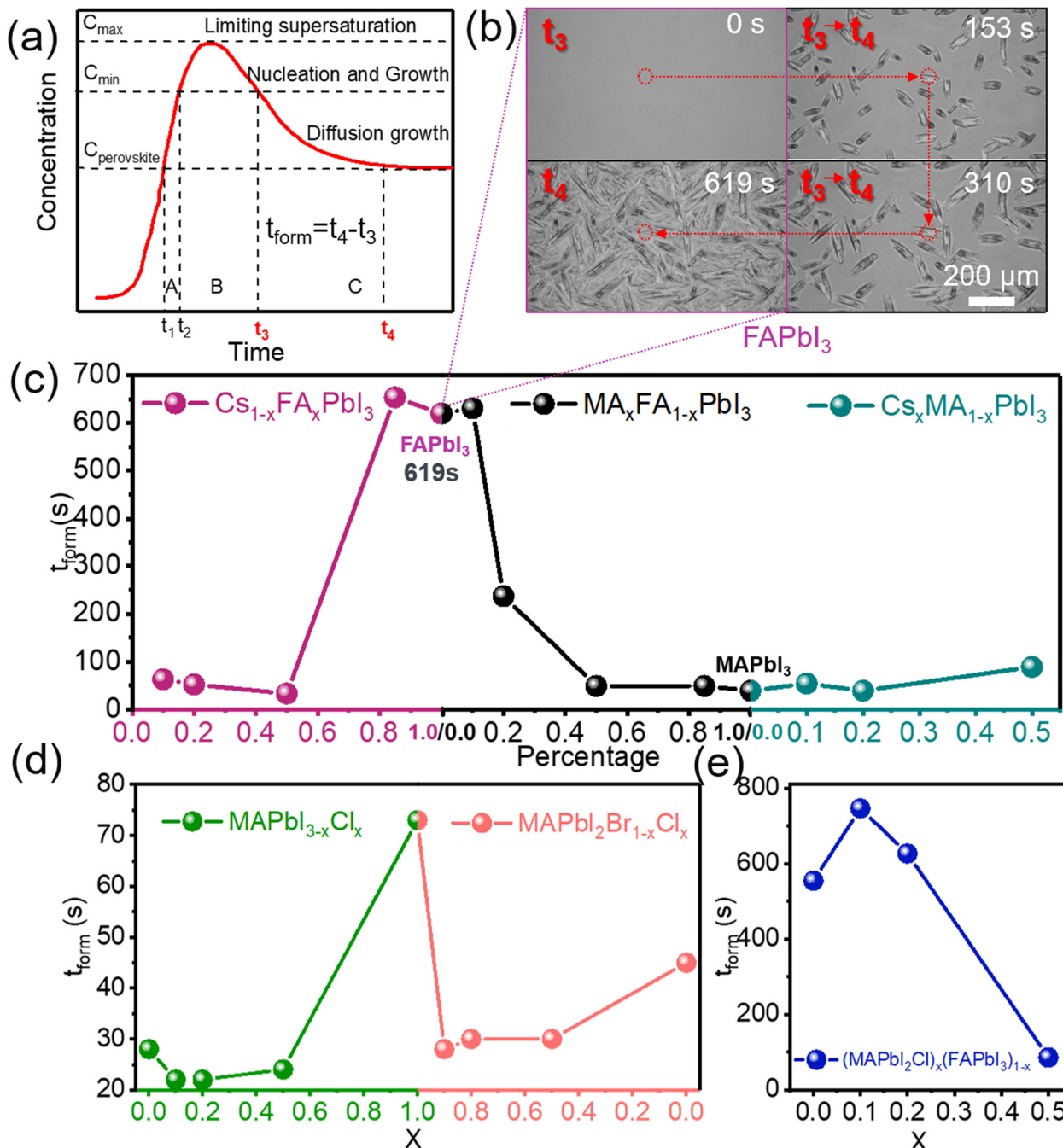
Fig. 1 Crystallization time until the perovskite is formed using different compositions. (a) LaMer model and (b) *in situ* optical microscopy images of the FAPbI$_3$ crystallization process. Crystallization formation time ($t_{form} = t_4 - t_3$) trend of perovskite with (c) different A-cations, (d) different halides, and (e) mixed A-cations and halides.

to dark yellow, indicating that MA diffuses at different time scales from FA.

In the fabrication process of perovskite films, annealing removes the solvent. It enhances the thermal movement of ions in the film, increasing the likelihood of bonding and forming perovskite grains.[31] Hence, after three days in nitrogen, the films are annealed at 100 °C for 10 min, and those with higher MA content become darker, indicating the formation of black MAPbI$_3$ perovskite. We then analyze the films using

scanning electron microscopy (SEM). The results presented in Fig. 2 demonstrate that the grain shape of perovskite remains the same before and after annealing, but MA$^+$ can form black phase perovskite by annealing in combination with PbI$_2$ after the crystallization process is completed.

To study the effects of intermediate on crystallization more closely, we compare three factors that influence perovskite crystallization: time, antisolvent, and annealing (Fig. S1, ESI†). The XRD pattern of MAPbI$_3$ shows low diffraction angles at
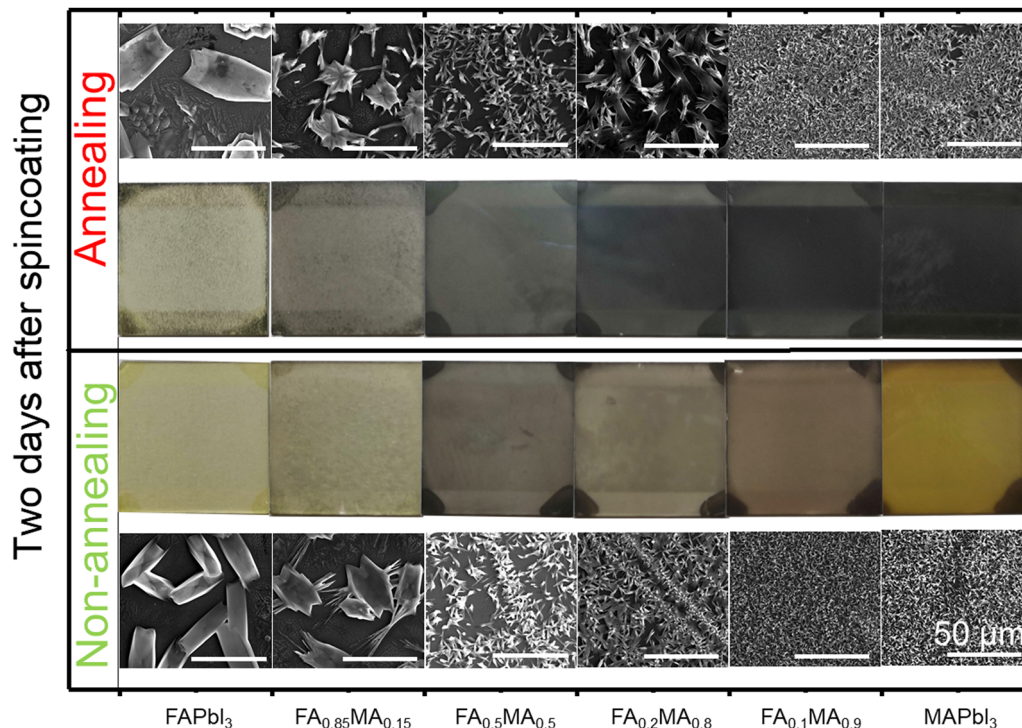
Fig. 2 Morphology of perovskite films with different A-cations with annealing at 100 °C (top) and without annealing (bottom). The scale bar is 50 μm.

6.55°, 7.21°, and 9.17° without annealing (or any other treatment) and subsequent storage in nitrogen for three days. This indicates that the films mainly consist of different structures formed by the intercalation of DMF and MAI molecules into a layered PbI_2 phase and MAI–PbI_2–DMSO intermediate phase.[32–34] Based on this kind of film, a pure perovskite phase could be obtained after annealing at 100 °C. However, when the $MAPbI_3$ film is annealed immediately after spin coating, the film still has an intermediate phase, as seen from the XRD in Fig. S1 (ESI†). This could not be eliminated even with the antisolvent treatment. The film of $FAPbI_3$ annealed immediately after spin-coating results in the precipitation of PbI_2, while annealing after three days of spin-coating results in a pure $FAPbI_3$ hexagonal phase as evidenced by XRD in Fig. S1 (ESI†). Adding an antisolvent treatment before annealing also results in a pure $FAPbI_3$ hexagonal phase. Also, the perovskite films with the smaller A-cation Cs^+, *i.e.* $CsPbI_3$, show no significant difference under various conditions.

To determine the results in Fig. S1 (ESI†), we investigate the initial adsorption of different A-cations using density functional theory to understand the interactions between A-cations and PbI_2 (0 0 1) surfaces (see Fig. 3a). Strong adsorption energy between molecules typically can increase steric effects and affect their movement. The adsorption energy calculation value of Cs on PbI_2 (0 0 1) surface is significantly higher compared to Rb and K. This aligns with the article Hu *et al.*,[35] which states that Cs reduces the defect density and charge complexation rate of the perovskite layer while Rb increases the carrier mobility. In the adsorption energy comparison in Fig. 3a (specific values are shown in Table S2 ESI,† and the calculation process Supplementary Note 3, ESI†), MA adsorption on the PbI_2
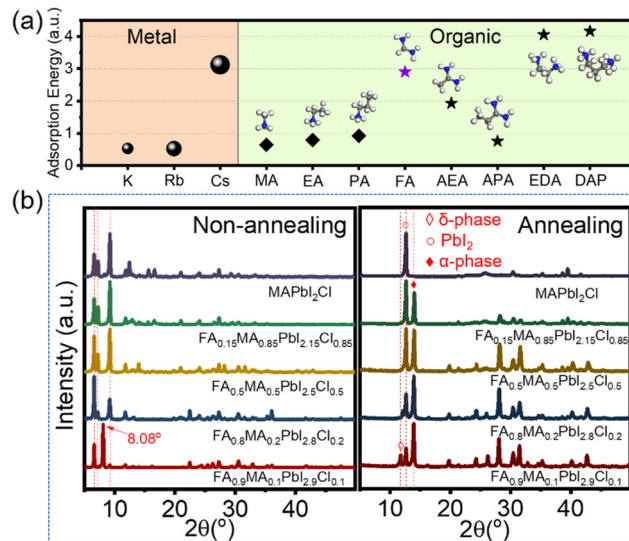

Fig. 3 (a) Adsorption energies of different A-cations on PbI_2 (0 0 1) surfaces using the following cations: K, Rb, Cs, MA(CH_3NH_3), EA($CH_3CH_2NH_3$), PA($CH_3CH_2CH_2NH_3$), FA($CH(NH_2)_2$), AEA($CH_3CH(NH_2)_2$), APA($CH_3CH_2CH-(NH_2)_2$), EDA($NH_3CH_2CH_2NH_3$), DAP($NH_3CH_2CH_2CH_2NH_3$). The diamond shape denotes a small molecule with a single amino group; the start denotes a small molecule with two amino groups. (b) The XRD pattern of MACl ratio affects the crystallization of $FAPbI_3$ perovskite intermediate phase (left) and films (right).

(0 0 1) surface is significantly lower than Cs and FA. The electron density distribution in Fig. S2 (ESI†) also shows significant surface electron density polarization of FA and Cs,

while analyzing the surface electron density of MA, it appears homogeneous and does not indicate any variations in its adsorption sites. Additionally, the evidence presented in Fig. 3a and Fig. S2 (ESI†) corroborates the observation in Fig. 2, *i.e.*, it is more probable for MA with low steric effects to merge with PbI_2 to form black phase perovskite.

In Fig. 3a, we analyze how the longer alkyl chain affects the adsorption energy. As we move from MA to ethylaminium (EA) and propylaminium (PA), the adsorption energy is slightly increased from 0.64 to 0.79 to 0.92 eV per molecule. However, the size of the A-cation also increases, making EA and PA unsuitable for 3D perovskites.

On the other hand, when the alkyl chain is extended from FA to 1-aminoethaniminium (AEA) to 1-aminopropyliminium (APA) based on a similar amidine group, the adsorption energy decreases significantly from 2.90 to 1.93 to 0.76 eV per molecule. Interestingly, if we turn the terminal group into two amino groups and extend the alkyl chain, the adsorption energy increases when comparing FA with ethylenediaminium (EDA) and 1,3-diaminopropanium (DAP) from 2.90 to 4.06 to 4.16 eV per molecule. These findings highlight the unique structure of FA, which makes it suited for stable single-phase perovskites.

According to the previous conclusion, since MA^+ can maintain a perovskite structure by inserting into the $[PbI_6]^{4-}$ scaffold even after grain formation, we used $FAPbI_3$ perovskite as the primary material and MA^+ as the crystallization aid to fabricate black phase $FAPbI_3$ perovskite. Due to the low boiling point at 225 °C under 15 mm Hg,[36,37] MACl is selected as a relatively easily removable crystallization aid to direct the formation of $FAPbI_3$ (Fig. 3b). We fabricate a series of $FA_{1-x}MA_xPbI_{3-x}Cl_x$ films and compare the phases of annealed and unannealed films three days after spin-coating in a nitrogen atmosphere. The XRD results exhibit that the unannealed films have significantly altered intermediate phases when the MA^+ ratio reached 20% (the peak at 8.08° disappeared except for $x = 0.1$), while the annealed films at 150 °C[38] did not exhibit the yellow phase of perovskite when the mole ratio of MA reached 50%. This result suggests that the MACl dopant range is between 0.2 and 0.5 molar ratio in which the intermediate phase is sufficient to support the formation of the pure phase $FAPbI_3$. The PbI_2 in the film mainly comes from the component residue after the volatilization of MACl, which is evident in the XRD of the component with $x = 1$. In Fig. S3 (ESI†), the zoom-in XRD patterns between 13° to 15° show that the peak of the black perovskite phase is shifted with the increase of MACl content in the precursor. According to Bragg's law, this may be attributed to a small angular distortion of the perovskite crystal plane caused by the residual PbI_2.

Interestingly, at $x = 0.5$, a black phase also forms spontaneously in the perovskite that is kept in nitrogen for three days without being annealed (Fig. 3b). Therefore, to define if the black-phase perovskite is $MAPbI_3$ or $FAPbI_3$, we compare two perovskite precursor ratios: 50 mol% MACl in 1.5 M $FAPbI_3$ and 50 mol% FACl in 1.5 M $MAPbI_3$. The films are then studied by XRD, UV-Vis, and SEM, as shown in Fig. S4 (ESI†). When the perovskite films are stored in nitrogen for three days after spin

coating and then annealing, the yellow and black phases of $FAPbI_3$ will appear in the film.[39,40] When the samples are annealed immediately after spin-coating, pure black phase perovskite is obtained from both formulations, as confirmed by XRD and UV-vis absorption curves (Fig. S4b, ESI†). Despite the changes in precursor concentration, the morphology of perovskite grain in the SEM images (Fig. S4c and d, ESI†) remains similar between the two formulations, indicating that perovskite is combined with A-cation in ionic form during the crystal formation process. Simply put, creating films with consistent components can be accomplished by using various compounds to make the same precursor solution, such as the precursor made from $FAPbI_3$ + MACl and $MAPbI_3$ + FACl. However, magnifying the XRD patterns at 13° to 15° (Fig. S5, ESI†) reveals that the presence of the yellow phase affects the crystal structure of the perovskite, which is consistent with Bragg's law. Analysis of the XRD peaks[41] shows that annealing the films of both precursors forms a single-component perovskite. Furthermore, an immediate annealing treatment at 150 °C yields a pure black-phase $FAPbI_3$ perovskite.

As discussed previously, when the ratio of A-cations, with respect to FA, exceeds 50% in the precursor, this causes the change of the perovskite grain shape; this is also seen in Fig. S4c and d (ESI†). According to Fig. 3b, $FAPbI_3$ converts into the black phase when the MACl concentration is greater than 20%. This result agrees with the report of Jeon *et al.*[42] Thus, the concentration of MACl in the precursor is set at 35% (a value between 20% and 50%) in the following study in this work. SEM images (Fig. S4c and d, ESI†) indicate that the films obtained from 1.5 M precursor could not fully cover the substrate, prompting us to increase the precursor concentration. The concentration of the precursor is 1.8 M to make perovskite films fully cover the substrate (Fig. S6, ESI†).

In our study, we also aim to investigate methods for passivating the surface of perovskite grains to improve their stability against water erosion. The effects of air humidity, annealing, and antisolvent treatments are examined on perovskite films. To study the effects of these treatments, we prepare wet perovskite films with and without antisolvent, and divided them into two groups: one placed in air overnight and the other in dry nitrogen. After annealing at 150 °C, we analyze the resulting films using XRD. Our results, as shown in Fig. S7 (ESI†), indicates that films processed with or without antisolvent and annealing in air overnight yield pure-phase perovskite, while other conditions lead to the formation of PbI_2 or the yellow phase perovskite.

Although annealing at 150 °C is necessary for the formation of black phase $FAPbI_3$, our results suggest that a random additive, which briefly forms an intermediate phase with the perovskite precursor and can be easily removed at a later stage, is favorable for the formation of the black phase of $FAPbI_3$. This additive can, *e.g.*, be water or oxygen from the air. However, it is important to note that water or oxygen will eventually decompose $FAPbI_3$, so we raise this point to discuss the underlying mechanism.

In summary, our experiments shows that ions combined with PbI_2 skeleton can stabilize black phase $FAPbI_3$, and that
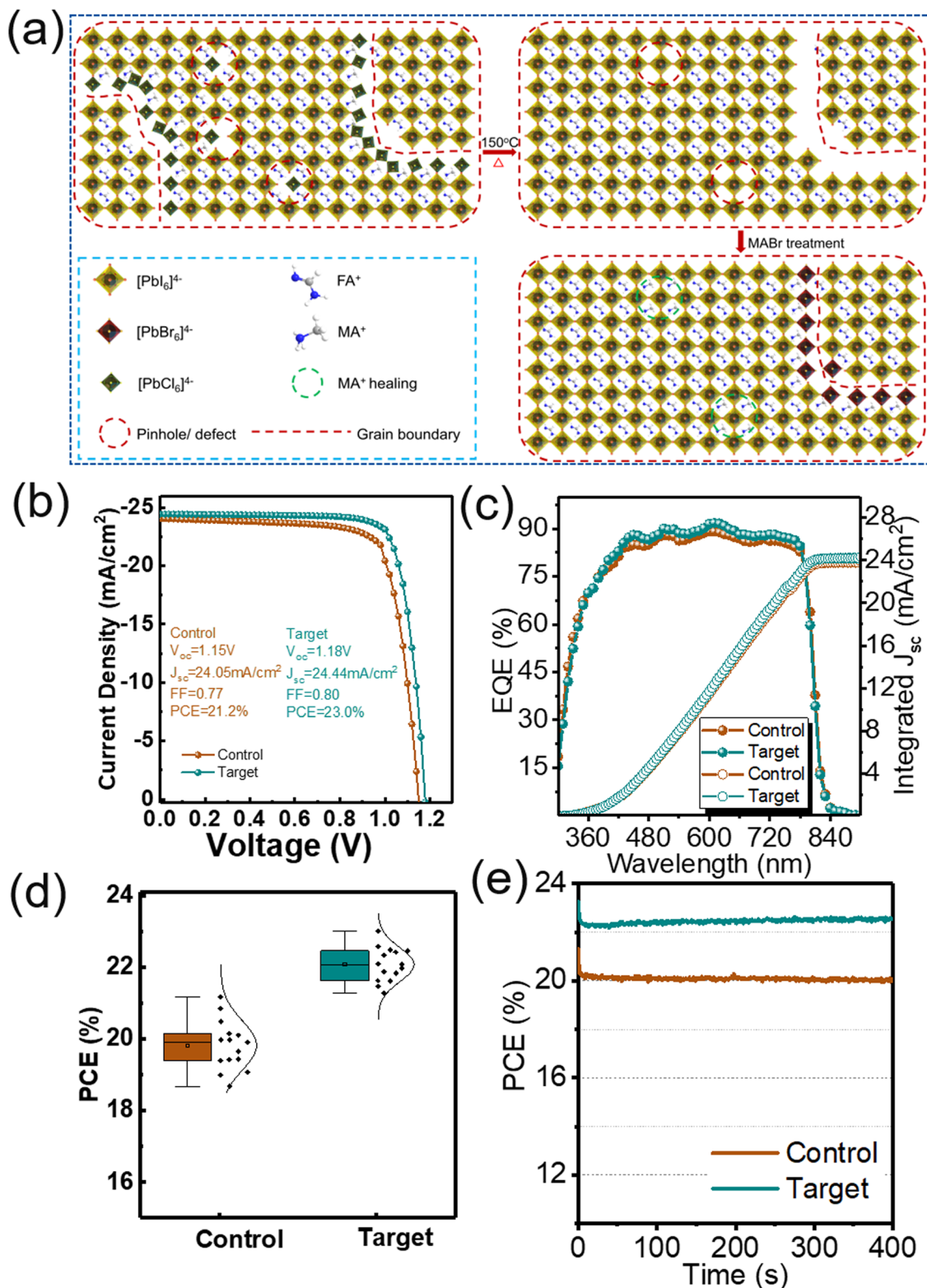
Fig. 4 (a) The mechanism of action of MA^+ and $(PbCl_6)^{4-}$ in perovskite crystals and MABr passivation. (b) Current density–voltage (J–V) curves, (c) EQE, (d) PCE box statistical chart and (e) maximum power point tracking of perovskite solar cells of pure $FAPbI_3$ (control) as well as $FAPbI_3$ with MABr passivated (target).

both doping and interfacial modifications can be effective methods for achieving this. These methods need to target the same location as the initial decomposition of perovskite by water and oxygen in the air.[43–45]

We optimize the crystallization of black phase $FAPbI_3$ by using the MACl dopant, which does not remain in the film after annealing at 150 °C. The mechanism by which MACl acts on perovskite crystals is elaborated in Fig. 4a. And the adsorption energy of MA on $PbBr_2$ (0 2 0) surface is higher than PbI_2 (0 0 1) surface, MABr is used as a passivation material for the $FAPbI_3$ layer for homogeneous doping for defect reduction. The specific values are shown in Table S2 (ESI†). Three-dimensional maps of the charge density difference for adsorption of an MA molecule on $PbBr_2$ (0 2 0) surface is shown in Fig. S8 (ESI†).

Therefore, we anticipate that the co-hybrid phase on the surface can create a protective shell around the $FAPbI_3$ grains, providing resistance against moisture. Our experimental results indicate that while the $FAPbI_3$ film (control) turned yellow after one week in air with 45% humidity, the $FAPbI_3$ films passivated with MABr (target) remained black (Fig. S9, ESI†). As demonstrated in Fig. S9 (ESI†), while the $FAPbI_3$ films exhibited degradation, the target film maintains large crystals within the film.

Based on the mechanism discussed, we fabricate solar cells with a structure of ITO/SnO_2/perovskite (~ 530 nm)/spiro-OMeTAD/Au to study the performance (the thickness of perovskite is measured by a profilometer as shown in Fig. S10, ESI†). The bandgap of the perovskite is at 1.50 eV. The champion PCE of the control devices is 21.2%, with a V_{oc} of 1.15 V, a J_{sc} of 24.05 mA cm^{-2}, and a FF of 0.77. The target devices with MABr show higher performance: the champion PCE reaches 23.0%, with a V_{oc} is 1.18 V, a J_{sc} is 24.44 mA cm^{-2}, and a FF of 0.80 (Fig. 4b). The champion devices show similar hysteresis behavior (Fig. S11, ESI†). The external quantum efficiencies (EQEs) of the cells are presented in Fig. 4c. Based on the EQE spectra, integral J_{sc} values of 23.90 and 24.31 mA cm^{-2} are obtained for control and target solar cells, respectively, consistent with the J–V measurements values. When MABr is used, the averaged PCE (15 cells) is improved from 19.8% to 22.0%, with an average V_{oc}, J_{sc}, and FF of 1.14 V, 24.33 mA cm^{-2}, and 0.79 (Fig. 4d and Fig. S12, ESI†). The maximum power point (MPP) tracking under AM 1.5G illumination for the best control and target devices shown in Fig. 4e indicates a stabilized PCE of 20.0% and 22.5%, respectively. These results confirm the advantage of the $FAPbI_3$:MABr film to the pure $FAPbI_3$ film.

Conclusions

The more controllable crystallization dynamics of perovskite enables the production of high-quality films, resulting in high-performance solar cells. Our work shows that $FAPbI_3$ has the longest crystallization formation time of all the pure phases of perovskite and can therefore be used to obtain films with low defect density. However, it tends to form the hexagonal non-perovskite polymorph, making it challenging for photovoltaic applications. After discussing the perovskite crystallization process, MACl is selected as the crystallizing aid to modulate the intermediate phase resulting in more controllable crystallization dynamics to fabricate black-phase perovskite films.

In addition, MABr is used to heal defects and passivate $FAPbI_3$ to obtain air-stable films. The perovskite solar cell fabricated using this strategy presents a high efficiency of 23.0%.

Experimental section

Material preparation

The chemicals and solvents were obtained commercially and used without further purification. SnO_2 colloid precursor (15% in H_2O colloidal dispersion) was purchased from Alfa Aesar. The organic cation halide salts for perovskite formamidinium iodide (FAI), formamidinium chloride (FACl), methylammonium iodide (MAI), methylammonium bromide (MABr), methylammonium chloride (MACl) were purchased from Greatcell Solar Materials. Lead iodide (PbI_2), Lead bromide ($PbBr_2$) was purchased from TCI. $FAPbI_3$ was purchased from Xi'an Polymer Light Technology Corp. Lithium bis(trifluoromethylsulphonyl) imide (Li-TFSI) (99.95%) and Cesium iodide (CsI) were purchased from Sigma-Aldrich. 2,2′,7,7′-tetrakis[N,N-di(4-methoxyphenyl)amino]-9,9′-spirobifluorene (Spiro-OMeTAD) (99.5%), 4-tert-butyl pyridine (tBP) (99.9%), and FK209 (Co(III) TFSI salt) (98%) were purchased from Advanced Election Technology CO, Ltd, TCI, and Dyesol, respectively. All solvents, including dimethyl sulfoxide (DMSO), dimethylformamid (DMF), diethyl ether (DE) were purchased from Sigma-Aldrich.

Device fabrication

Patterned ITO substrates (7 Ω sq^{-1}, AGC) were ultrasonically cleaned with 2% Hellmanex water solution, deionized water, acetone, and IPA. Before use, the as-cleaned substrates were further cleaned with UV ozone treatment for 15 min. Then the SnO_2 solution (2.67%, diluted by water) was spin-coated onto the substrates at 3000 rpm for 25 s and annealed on a hot plate at 150 °C for 30 min under ambient atmosphere. After cooling down to room temperature, the substrates were treated with UV ozone for 20 min. 1.8 M $FAPbI_3$: MACl (1 : 0.35) nominal stock solution in 1 ml DMF : DMSO 8 : 1, calculate the actual M from the density of the solution. It needs to be ensured that the stock solution is clear with no residual of powder in the solution and under the lid. The stock solutions of $FAPbI_3$ was warmed overnight at 25 °C in the shaker and then left to cool to room temperature for 30 min before usage. The perovskite precursor solution was then spin-coated onto SnO_2 in a nitrogen-filled glove box with a two-step program at 1000 and 6000 rpm for 5 and 27 s, respectively. During the spin-coating process, an antisolvent was dripped on the spinning substrate slowly at 5 s before the end of the program. The volume of antisolvent DE was 300 µL. After spin-coating, the film needs to be annealed at 150 °C for 15 min with an additional post-annealing at 100 °C for 30 min. After cooling down to room temperature, the spiro-OMeTAD solution (73.2 mg in 1 mL ANS) doped with 18 µL of Li-TFSI (520 mg mL^{-1} in ACN), 29 µL of FK209 Co (III) TFSI salt (300 mg mL^{-1} in ACN), and 29 µL tBP was spin-coated at 4000 rpm for 30 s. Finally, 100 nm of gold was thermally evaporated under a pressure of 10^{-6} mbar as the back electrode.

For MABr passivation, 5 mg mL^{-1} MABr dissolved in IPA and spin-coated at 6000 rpm on the FAPbI$_3$ film at room temperature, the volume of the dropping was 200 μL, followed by annealing at 100 °C for 10 min.

Characterizations

The surface morphology of the electrode was characterized by scanning electron microscopy (SEM) operated at 20 KV 3.2 nA in a Thermo Fischer SCIOS Dual-beam microscope. The solar cells were characterized using an LED Solar Simulator (Wavelabs Solar Metrology Systems) with a certified AM1.5G spectrum (100 mW cm^{-2}). The J–V characteristics were measured in both reverse and forward direction with a constant scan rate of ~10 mV s^{-1} (Keithley 2400 source measurement unit). The UV-Vis absorbance spectra of the perovskite films were measured with a PerkinElmer LAMBDA 0101. The perovskite films' crystallinity was examined by an X-ray diffraction (XRD, SmartLab SE from Rigaku) machine with a HyPix-400 (2D HPAD) detector.

Author contributions

M. S. directed and supervised the research. W. Z. and M. S. conceived the idea. W. Z. designed the experiments. W. Z., W. F., K.-L. W. and M. L. fabricated and characterized perovskite films and devices. K. W. conducted the SEM measurements. M. M. B. conducted the XRD measurements. W. Z., W. F., K.-L. W. and M. L. performed the device performance measurements. W. Z., W. F. and M. L. participated in the data analysis and result discussions. W. Z. wrote the first draft of the manuscript with input from M. S. All authors contributed to the discussion, commented, reviewed and approved of the paper. M. L. and M. S. provided expertise and supervised the work.

Conflicts of interest

The authors declare no competing interests.

Acknowledgements

References

1 NREL, Best Research-Cell Efficiency Chart, 09/12/2023.

2 P. P. Boix, S. Agarwala, T. Ming Koh, N. Mathews and S. G. Mhaisalkar, *J. Phys. Chem. Lett.*, 2015, **6**(5), 898–907.

3 P. K. Nayak, S. Mahesh, H. J. Snaith and D. Cahen, *Photovoltaic Solar Cell Technologies: Bounds and Challenges*, 2019.

4 S. D. Stranks, G. E. Eperon, G. Grancini, C. Menelaou, M. J. P. Alcocer, T. Leijtens, L. M. Herz, A. Petrozza and H. J. Snaith, *Electron-Hole Diffusion Lengths Exceeding 1 Micrometer in an Organometal Trihalide Perovskite Absorber*, 2013, vol. 342.

5 R. E. Brandt, J. R. Poindexter, P. Gorai, R. C. Kurchin, R. L. Z. Hoye, L. Nienhaus, M. W. B. Wilson, J. A. Polizzotti, R. Sereika, R. Žaltauskas, L. C. Lee, J. L. Macmanus-Driscoll, M. Bawendi, V. Stevanović and T. Buonassisi, *Chem. Mater.*, 2017, **29**, 4667–4674.

6 Z. Li, M. Yang, J. S. Park, S. H. Wei, J. J. Berry and K. Zhu, *Chem. Mater.*, 2016, **28**, 284–292.

7 C. J. Bartel, C. Sutton, B. R. Goldsmith, R. Ouyang, C. B. Musgrave, L. M. Ghiringhelli and M. Scheffler, *New tolerance factor to predict the stability of perovskite oxides and halides*, 2019.

8 T. Sato, S. Takagi, S. Deledda, B. C. Hauback and S.-I. Orimo, *Sci. Rep.*, 2016, **6**, 23592.

9 W. Travis, E. N. K. Glover, H. Bronstein, D. O. Scanlon and R. G. Palgrave, *Chem. Sci.*, 2016, **7**, 4548–4556.

10 K. Miyata, T. L. Atallah and X.-Y. Zhu, *Lead halide perovskites: Crystal-liquid duality, phonon glass electron crystals, and large polaron formation*, 2017.

11 N. Arora, A. Greco, S. Meloni, A. Hinderhofer, A. Mattoni, U. Rothlisberger, J. Hagenlocher, C. Caddeo, S. M. Zakeeruddin, F. Schreiber, M. Graetzel, R. H. Friend and M. I. Dar, *Commun. Mater.*, 2022, **3**, 22.

12 Y. Wu, A. Islam, X. Yang, C. Qin, J. Liu, K. Zhang, W. Peng and L. Han, *Energy Environ. Sci.*, 2014, **7**, 2934–2938.

13 Q. A. Akkerman, E. Bladt, U. Petralanda, Z. Dang, E. Sartori, D. Baranov, A. L. Abdelhady, I. Infante, S. Bals and L. Manna, *Chem. Mater.*, 2019, **31**, 2182–2190.

14 T. Dammak, S. Elleuch, H. Bougzhala, A. Mlayah, R. Chtourou and Y. Abid, *J. Lumin.*, 2009, **129**, 893–897.

15 W. Peng, L. Wang, B. Murali, K. T. Ho, A. Bera, N. Cho, C. F. Kang, V. M. Burlakov, J. Pan, L. Sinatra, C. Ma, W. Xu, D. Shi, E. Alarousu, A. Goriely, J. H. He, O. F. Mohammed, T. Wu and O. M. Bakr, *Adv. Mater.*, 2016, **28**, 3383–3390.

16 Z. Chen, B. Turedi, A. Y. Alsalloum, C. Yang, X. Zheng, I. Gereige, A. Alsaggaf, O. F. Mohammed and O. M. Bakr, *ACS Energy Lett.*, 2019, **4**, 1258–1259.

17 Y. Liu, Y. Zhang, Z. Yang, D. Yang, X. Ren, L. Pang and S. F. Liu, *Adv. Mater.*, 2016, **28**, 9204–9209.

18 Y. Wang, X. Sun, Z. Chen, Y. Y. Sun, S. Zhang, T. M. Lu, E. Wertz and J. Shi, *Adv. Mater.*, 2017, **29**, 1702643.

19 Y. Liu, J. Sun, Z. Yang, D. Yang, X. Ren, H. Xu, Z. Yang and S. F. Liu, *Adv. Opt. Mater.*, 2016, **4**, 1829–1837.

20 J. Chen, D. J. Morrow, Y. Fu, W. Zheng, Y. Zhao, L. Dang, M. J. Stolt, D. D. Kohler, X. Wang, K. J. Czech, M. P. Hautzinger, S. Shen, L. Guo, A. Pan, J. C. Wright and S. Jin, *J. Am. Chem. Soc.*, 2017, **139**, 13525–13532.

21 A. A. Zhumekenov, V. M. Burlakov, M. I. Saidaminov, A. Alofi, M. A. Haque, B. Turedi, B. Davaasuren, I. Dursun, N. Cho, A. M. El-Zohry, M. De Bastiani, A. Giugni, B. Torre, E. Di Fabrizio, O. F. Mohammed, A. Rothenberger, T. Wu, A. Goriely and O. M. Bakr, *ACS Energy Lett.*, 2017, **2**, 1782–1788.

22 Z. Shen, Q. Han, X. Luo, Y. Shen, T. Wang, C. Zhang, Y. Wang, H. Chen, X. Yang, Y. Zhang and L. Han, *Energy Environ. Sci.*, 2022, **15**, 1078–1085.

23 W. W. Zuo, Y. G. Yang, W. F. Fu, M. Li, M. Malekshahi Byranvand, D. di Girolamo, J. Pascual, M. Q. Li, L. N. Li, A. Abate, M. Saliba and Z. K. Wang, *ACS Mater. Lett.*, 2022, **4**, 448–456.

24 H. Lu, Y. Liu, P. Ahlawat, A. Mishra, W. R. Tress, F. T. Eickemeyer, Y. Yang, F. Fu, Z. Wang, C. E. Avalos, B. I. Carlsen, A. Agarwalla, X. Zhang, X. Li, Y. Zhan, S. M. Zakeeruddin, L. Emsley, U. Rothlisberger, L. Zheng, A. Hagfeldt and M. Grätzel, *Science*, 2020, **370**, 74.

25 C. B. Whitehead, S. O. Zkar and R. G. Finke, *Chem. Mater.*, 2019, **31**(18), 7116–7132.

26 V. K. Lamer and R. H. Dinegar, *J. Am. Chem. Soc.*, 1950, **72**, 4847–4854.

27 M. Jung, S.-G. Ji, G. Kim and S. il Seok, *Chem. Soc. Rev.*, 2019, **48**, 2011–2038.

28 J.-P. Correa-Baena, M. Saliba, T. Buonassisi, M. Grätzel, A. Abate, W. Tress and A. Hagfeldt, *Science*, 2017, **358**, 739–744.

29 A. Amat, E. Mosconi, E. Ronca, C. Quarti, P. Umari, M. K. Nazeeruddin, M. Grä and F. De Angelis, *Nano Lett.*, 2014, **14**, 3616.

30 K. L. Wang, Z. H. Su, Y. H. Lou, Q. Lv, J. Chen, Y. R. Shi, C. H. Chen, Y. H. Zhou, X. Y. Gao, Z. K. Wang and L. S. Liao, *Adv. Energy Mater.*, 2022, **12**, 202201274.

31 C. Bi, Y. Shao, Y. Yuan, Z. Xiao, C. Wang, Y. Gao and J. Huang, *J. Mater. Chem. A*, 2014, **2**, 18508–18514.

32 N. Joong Jeon, J. Hong Noh, Y. Chan Kim, W. Seok Yang, S. Ryu and S. il Seok, *Nat. Mater.*, 2014, **13**, 897–903.

33 A. A. Petrov, N. Pellet, J. Y. Seo, N. A. Belich, D. Y. Kovalev, A. V. Shevelkov, E. A. Goodilin, S. M. Zakeeruddin, A. B. Tarasov and M. Graetzel, *Chem. Mater.*, 2017, **29**, 587–594.

34 D. Shen, X. Yu, X. Cai, M. Peng, Y. Ma, X. Su, L. Xiao and D. Zou, *J. Mater. Chem. A*, 2014, **2**, 20454–20461.

35 Y. Hu, E. M. Hutter, P. Rieder, I. Grill, J. Hanisch, M. F. Aygüler, A. G. Hufnagel, M. Handloser, T. Bein, A. Hartschuh, K. Tvingstedt, V. Dyakonov, A. Baumann, T. J. Savenije, M. L. Petrus and P. Docampo, *Adv. Energy Mater.*, 2018, **8**, 1703057.

36 C. Zhang, Z. Li, J. Liu, Y. Xin, Z. Shao, G. Cui and S. Pang, *ACS Energy Lett.*, 2018, **3**, 1801–1807.

37 J. Chae, Q. Dong, J. Huang and A. Centrone, *Nano Lett.*, 2015, **15**, 8114–8121.

38 P. Ahlawat, A. Hinderhofer, E. A. Alharbi, H. Lu, A. Ummadisingu, H. Niu, M. Invernizzi, S. M. Zakeeruddin, M. I. Dar, F. Schreiber, A. Hagfeldt, M. Grätzel, U. Rothlisberger and M. Parrinello, *Sci. Adv.*, 2021, **7**, eabe3326.

39 D. X. Yuan, A. Gorka, M. F. Xu, Z. K. Wang and L. S. Liao, *Phys. Chem. Chem. Phys.*, 2015, **17**, 19745–19750.

40 Y. Zhang, S. G. Kim, D. Lee, H. Shin and N. G. Park, *Energy Environ. Sci.*, 2019, **12**, 308–321.

41 D. X. Yuan, A. Gorka, M. F. Xu, Z. K. Wang and L. S. Liao, *Phys. Chem. Chem. Phys.*, 2015, **17**, 19745–19750.

42 N. J. Jeon, H. Na, E. H. Jung, T. Y. Yang, Y. G. Lee, G. Kim, H. W. Shin, S. il Seok, J. Lee and J. Seo, *Nat. Energy*, 2018, **3**, 682–689.

43 J. Jiang, Q. Wang, Z. Jin, X. Zhang, J. Lei, H. Bin, Z. G. Zhang, Y. Li and S. F. Liu, *Adv. Energy Mater.*, 2018, **8**, 1701757.

44 T. Miyasaka, A. Kulkarni, G. M. Kim, S. Öz and A. K. Jena, *Adv. Energy Mater.*, 2020, **10**, 1902500.

45 F. Gao, Y. Zhao, X. Zhang and J. You, *Adv. Energy Mater.*, 2020, **10**, 1902650.